Effect of Anion Species in Early Stage of SEI Formation Process

Sonoki, Hidetoshi

Matsui, Masaki

Imanishi, Nobuyuki

(Citation)
Journal of The Electrochemical Society,166(15):A3593-A3598

(Issue Date)
2019-10-23

(Resource Type)
journal article

(Version)
Version of Record

Effect of Anion Species in Early Stage of SEI Formation Process

Hidetoshi Sonoki, [1,*] **Masaki Matsui,** [2,**,z] **and Nobuyuki Imanishi** [1,**]

[1]*Department of Chemistry for Materials, Mie University, Tsu, Mie 514-8507, Japan*
[2]*Department of Chemical Science and Engineering, Kobe University, Nada-ku, Kobe, Hyogo 657-8501, Japan*

We investigate the early stage of the solid electrolyte interphase (SEI) layer formation process in four electrolyte solutions, using electrochemical quartz crystal microbalance (EQCM) and X-ray photoelectron spectroscopy (XPS). The EQCM result proves that the $LiBH_4$ in THF solution form a negligible amount of SEI layer. The SEI formation process of the $LiPF_6$ solution occurs at 2.3 V vs. Li, and the SEI layer continuously grows even during the anodic scan. The electrolyte solutions containing LiTFSA form SEI layer around 1.5 V vs. Li. The XPS study shows that the SEI layer formed at high electrode potential, in the electrolyte containing $LiPF_6$ forms a dense LiF layer. The LiTFSA solution forms a thick SEI layer containing organic components such as lithium alkyl carbonate or polyether.

 [DOI: 10.1149/2.0191915jes]

Manuscript submitted August 29, 2019; revised manuscript received October 2, 2019. Published October 23, 2019.

Lithium-ion batteries are widely used energy storage devices because of their long cycle life and high specific energy. With the spread of their applications from portable electronics through large electric supply stations, the demands for high-energy rechargeable batteries have been continuously increasing.[1–3] A typical strategy to develop high-energy rechargeable batteries is using high-capacity anodes, such as lithium metal and lithium alloys.[4,5] There remains a lot of problems to utilize lithium metal or alloys as battery anodes, for the widespread applications.

The lithium metal electrodes suffer from the unavoidable dendritic deposition of lithium metal during the charging process. The lithium dendrite leads the internal short circuit of the cell, resulting in safety incidents. The inhomogeneous solid electrolyte interphase (SEI), on the lithium metal anode causes dendritic growth.[6] Since salts, solvents, and impurities of the electrolyte are simultaneously reduced, typical SEI layer has an inhomogeneous or mosaic morphology.[7–9] The inhomogeneous morphology of the SEI layer induces a locally focused current that leads to dendritic growth.[10,11] To suppress the dendritic growth, researchers have tried physical protection of lithium anode using solid electrolytes[12] and forming stable SEI layer using various electrolyte component materials, such as electrolyte salts,[11] solvents,[13] and additives.[14,15] We previously reported that fluoroethylene carbonate (FEC) stabilizes the surface layer, and a solvate ionic liquid delays the dendrite formation.[16,17] However, the dendrite formation still remains as a fundamental challenge on the lithium metal anodes.[13,18–20]

In the case of the alloy/intermetallic anodes, the volume expansion and shrinkage of the active material leads pulverization of the particles during the charging and discharging processes. The pulverized particles are isolated from the electronic/ionic conduction paths and deteriorate the cycle life.[5,21] Many researchers have attempted to suppress the deterioration using nano-sized and structure-controlled active materials,[22,23] strong adhesive binders,[24,25] and electrolyte additives.[26–29] Some film forming additives, such as vinylene carbonate (VC) and FEC, improve the cycling performance of lithium–silicon alloy anodes. The VC forms polymerized surface film and reduce the formation of lithium fluoride (LiF) in the SEI layer.[28] The FEC produces an SEI layer with low charge-transfer resistance, and improves the cycling performance of a lithium–silicon composite anode.[30] Among the above studies, the surface film suppresses further decomposition of the electrolyte and physically protects the electrode surface. Therefore the formation of stable and flexible surface film becomes one of the major strategies to improve the cycling performance of the high-capacity anodes.

On the other hand, we recently found that an electrolyte solution containing lithium borohydride ($LiBH_4$) remarkably improve the cycling performance of a lithium–bismuth intermetallic anode.[31] Since the $LiBH_4$ is a strong reducing agent, the SEI formation is significantly suppressed in the $LiBH_4$ solution, as a consequence, the electronic/ionic conduction paths in the composite electrode are maintained even after the pulverization of the intermetallic compounds. We also confirmed a decrease of the SEI formation using in situ Fourier transform infrared (FTIR) spectroscopy. Therefore we think the suppression of the SEI layer is an effective strategy to utilize the high capacity anodes. There remains a question, however, whether an SEI layer exists in the $LiBH_4$ solution or not, because the in situ FTIR spectra also detect the structural changes of the electrolyte solution at the vicinity of the electrode. Hence, we need to explore other methodology to characterize the SEI layer in the $LiBH_4$ solution. Variety of analytical techniques, such as electrochemical quartz crystal microbalance (EQCM),[32,33] X-ray photoelectron spectroscopy (XPS),[33–35] FTIR,[13,34] electrochemical impedance spectroscopy (EIS),[7,30,36] and atomic force microscopy (AFM)[10] have also been employed to characterize the SEI layer. Among these techniques, the EQCM is a powerful technique to quantify the amount of the SEI layer.

In the present study, we attempted to characterize and quantify the SEI layer produced in electrolyte solutions containing various electrolyte salts, using EQCM and XPS, mainly focusing on the early stage of the SEI formation process. Firstly we confirmed that the $LiBH_4$-based electrolyte forms a pseudo-SEI-free interphase. We also investigate how the conventional anion species, such as hexafluorophosphate (PF_6^-) anion and bis(trifluoromethanesulfonyl)amide anion ($TFSA^-$) affects to early stage of the SEI layer formation process.

Experimental

We conducted a comparative study of the SEI formation process using four electrolyte solutions: 2.0 mol L^{-1} $LiBH_4$ in THF ($LiBH_4$/THF), 1.0 mol L^{-1} $LiPF_6$ in ethylene carbonate–diethyl carbonate (50:50 vol%) ($LiPF_6$/EC–DEC), 1.0 mol L^{-1} LiTFSA in EC–DEC (50:50 vol%) (LiTFSA/EC–DEC), and 1.0 mol L^{-1} LiTFSA in diethylene glycol dimethyl ether (LiTFSA/diglyme). $LiBH_4$/THF (Sigma-Aldrich, MO) and $LiPF_6$/EC–DEC (lithium battery grade (LBG), Kishida Chemical, Japan) were used as received. The LiTFSA/EC–DEC and the LiTFSA/diglyme were prepared according to the following procedure: a LiTFSA (Wako Pure Chemical Industries, Japan) was dried under vacuum at 150°C for 8 h before usage; an EC–DEC (50:50 vol%, LBG, Kishida Chemical, Japan) and a diglyme (anhydrous, 99.5%, Sigma-Aldrich, MO) were dried over an activated molecular sieve (Nacalai Tesque, Japan); the dried LiTFSA was dissolved in the solvents and stirred for 24 h to obtain the desired solutions. The electrolyte solutions were stored and handled in

*Electrochemical Society Student Member.
**Electrochemical Society Member.
[z]E-mail: matsui@godzilla.kobe-u.ac.jp

a dried and argon-filled glove box. The water content in the solutions except for $LiBH_4$/THF was estimated to be <20 ppm with a Karl Fischer moisture titrator (MKC-510, Kyoto Electronics Manufacturing, Japan).

We conducted the EQCM measurements using a potentiostat/galvanostat (ECstat-301, EC Frontier, Japan) with a QCM system (QCM922A, Seiko EG&G, Japan). An AT-cut 9.04 MHz quartz crystal with copper electrode (QA-A9M-CU, Seiko EG&G, Japan) was employed as the working electrode in a three-electrode EQCM cell. Lithium foil (Honjo Metal, Japan) was used as the counter and the reference electrode. We performed EQCM cyclic voltammetry at a scan rate of 10 mV s^{-1} between open circuit potential and 0.1 V vs. Li to investigate the surface layer formation behavior under ambient temperature in the argon-filled glove box. The mass change per unit surface area of the working electrode $\Delta m/A$, which represents the amount of the SEI layer, was estimated by Sauerbrey equation.[37]

Potentiostatic measurements were performed at 0.5 or 1.5 V vs. Li for 24 h to prepare the surface layer for the XPS analyses. A copper foil (99+%, Nilaco, Japan) was employed as the working electrode in a conventional three-electrode cell. A lithium foil (Honjo Metal, Japan) was used as the counter and the reference electrode. After the measurement, the copper electrode was rinsed with a 1,2-dimethoxyethane (LBG, Kishida Chemical, Japan) for the $LiBH_4$/THF and the LiTFSA/diglyme, or rinsed with a DEC (LBG, Kishida Chemical, Japan) for the $LiPF_6$/EC–DEC and the LiTFSA/EC–DEC. The electrode was subsequently dried under vacuum to remove the solvents. The prepared sample was loaded into a spectrometer with a transfer vessel preventing exposure to air and moisture.

The XPS spectra for the samples were obtained using an X-ray photoelectron spectrometer (ESCA-3400, Shimadzu, Japan). The acceleration voltage and the emission current of Mg $K\alpha$ X-ray gun were 10 kV and 20 mA respectively. Depth profiles were collected after each argon ion etching. The etching rate is >4.0 nm min^{-1} based upon SiO_2. After the measurement, a Shirley-type background was applied to all the spectra. The spectra were curve-fitted by a combination of 70% Gaussian and 30% Lorenztian model curves. All figures in this article were generated using Matplotlib and Pandas Python-based libraries.[38,39]

Results and Discussion

At first, we performed EQCM cyclic voltammetry to examine the surface layer formation behavior in the electrolyte solutions. Figure 1 shows cyclic voltammograms (top), differential mass change–potential graphs at the first cathodic sweep (middle), and mass change–potential graphs (bottom) in the four electrolyte solutions. The darker color of the charts represents the earlier cycle of the EQCM cyclic voltammetry. In all cases, the significant increases in electrode mass are observed with the cathodic current peaks during the first cycle, and the mass changes are mostly irreversible. The irreversible mass change, the value of $\Delta m/A$ at the end of each cycle, decreases as cycled. The cyclic voltammograms after the second cycle show better reversibility, and the peak positions are different from those in the first cycle. Therefore, we suspect the surface layer is mostly formed in the first cycle.

As we expected, the $LiBH_4$/THF solution forms the smallest amount of the surface layer. As seen in Figure 1a, $\Delta m/A$ gradually decreases at the beginning of the first cycle, because the $LiBH_4$, which is typically used as the reduction agent, reduces the native oxide layer of the copper electrode. The first mass increase simultaneously appears with the cathodic current at 1.2 V vs. Li. We observe differential mass change peaks at the same potentials where the cathodic peaks are observed. The irreversible mass change at the first cycle was 0.02 μg cm^{-2}. The amount of the surface layer in $LiBH_4$/THF is a hundred times smaller compared with the other three electrolyte solutions. Furthermore, the mass change–potential graph after the second cycle also shows reversible behavior. Thus, we conclude that $LiBH_4$/THF is effective to suppress the surface layer formation and might achieve to form a pseudo-SEI-free interphase. The EQCM result of the $LiBH_4$ solution quantitatively proves the pseudo-SEI-free model, which we proposed in our previous paper.[31]

In the case of $LiPF_6$/EC–DEC, the mass increase of the copper electrode begins at a surprisingly high electrode potential of 2.3 V vs. Li during the initial cathodic sweep. The mass increase of the electrode is observed at the same electrode potential we identify the cathodic current peak. As shown in Figures 1b and 1c, the first significant irreversible increase in mass is observed from 2.3 to 1.7 V vs. Li in $LiPF_6$/EC–DEC, whereas $\Delta m/A$ began to increase at 1.2 V vs. Li in LiTFSA/EC–DEC. Even though $LiPF_6$ and the LiTFSA are dissolved

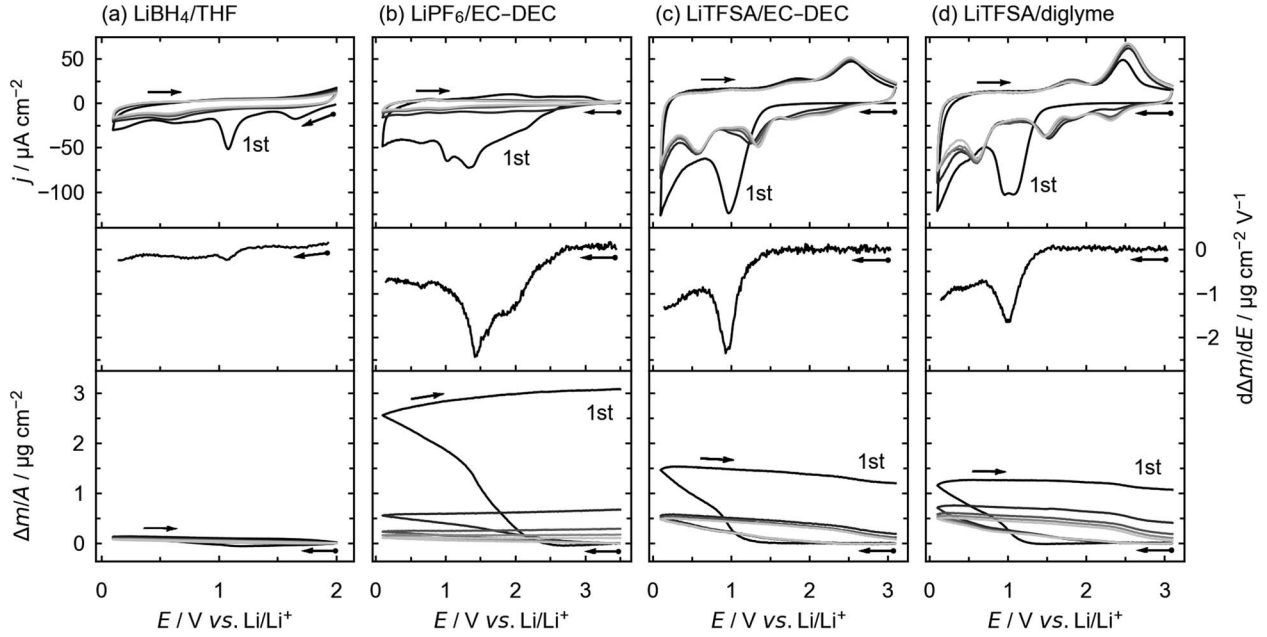

Figure 1. EQCM measurement results for the four electrolyte solutions; Cyclic voltammograms (top), differential mass change–potential graphs at the first cathodic sweep (middle), and mass change–potential graphs (bottom) in (a) 2.0 mol L^{-1} $LiBH_4$ in THF, (b) 1.0 mol L^{-1} $LiPF_6$ in EC–DEC, (c) 1.0 mol L^{-1} LiTFSA in EC–DEC, and (d) 1.0 mol L^{-1} LiTFSA in diglyme.

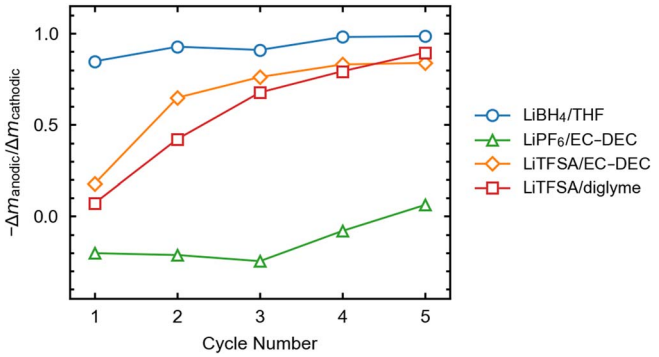

Figure 2. Reversible mass change during the EQCM cyclic voltammetry for the initial 5 cycles.

Table I. XPS peak assignments for the surface layer which formed on potentiostatic measurements.

	Binding energy/eV				
Component	C 1s	O 1s	Li 1s	B 1s	F 1s
Hydrocarbon	284.8				
Polyether	285.2–286.7	533.0			
$ROCO_2Li$	287.2–290.0	532	55		
Li_2CO_3	289.0–290.0	532	55		
Li_2O		529.5	53.5		
$LiBO_2$		530.4	55	191.5	
$LiBH_4$			55	188.0	
LiF			56.0		684.5–685.5
$LiPF_6$			56.7		686.6
LiTFSA			55		688.7

in the same solvent, EC–DEC (50:50 vol%), the onset potentials have a large gap. Thus, we think the cathodic current and the increase in mass above 1.2 V vs. Li in $LiPF_6$/EC–DEC could be corresponding to the reductive decomposition of PF_6^- anions and the surface layer formation. The irreversible mass change at the first cycle was 3.07 μg cm^{-2}, which is higher than that in the other three electrolyte solutions. Though the current observed in the cyclic voltammogram after the second cycle is almost negligible, the $\Delta m/A$ continuously increases. Accordingly, a relatively large amount of surface layer is formed in $LiPF_6$/EC–DEC.

The electrochemical behaviors of the LiTFSA/EC–DEC and the LiTFSA/diglyme are similar to each other. The electrode mass increases at 1.2 V vs. Li and below, which the cathodic current peak appears, as shown in Figures 1c and 1d. The current density is higher than that at the same potential in $LiPF_6$/EC–DEC. Hence, most of the cathodic current and the increase in $\Delta m/A$ could be assigned to the reductive decomposition of $TFSA^-$ anions and surface layer formation. After the second cycle, some cathodic peaks, not observed in $LiPF_6$/EC–DEC, appear at 0.6, 1.4, 1.8, and 2.3 V vs. Li. We calculated mass per mole of the electron from two potential ranges, 0.4–0.8 V vs. Li and 1.2–1.6 V vs. Li, as ≈6.9 g mol^{-1} that is close to the atomic weight of lithium, 6.94. Therefore, we ascribe the current peaks at 0.6 V vs. Li and 1.4 V vs. Li to conversion reactions of copper oxide.[40]

The EQCM cyclic voltammograms revealed that the surface layer formation behavior is strongly dependent upon anions in the electrolyte solutions. The $LiBH_4$/THF solution forms a tiny amount of the surface layer because of the excellent reductive stability of $LiBH_4$. In contrast, $LiPF_6$/EC–DEC produces the most significant amount of the surface layer at a relatively high electrode potential. It is said that $LiPF_6$-based electrolyte solution begins to decompose on carbonaceous electrodes below 1.0 V vs. Li.[41,42] However, several research groups reported that the electrolyte solution is also decomposed above 1.0 V vs. Li to form a surface layer on several substrates.[43–46] The LiTFSA-based electrolyte solutions produce thinner layer than the $LiPF_6$-based electrolyte. Although LiTFSA/diglyme employed the ether-based solvent as with $LiBH_4$/THF, only the $LiBH_4$-based electrolyte solution showed excellent reversibility in the electrode mass. The SEI formation is generally dominated by the decomposition of the solvent.[47–49] However, the above results suggest that the effect of the anions is higher than that of the solvents.

We evaluated the reversibility of the mass change during each CV cycle, as shown in Figure 2. The value of $-\Delta m_{anodic}/\Delta m_{cathodic}$ was calculated by the following equation,

$$-\Delta m_{anodic}/\Delta m_{cathodic} = -(\Delta m_{end} - \Delta m_{switch})/(\Delta m_{switch} - \Delta m_0), \quad [1]$$

where Δm_{end} is the mass change at the end of each cycle, Δm_{switch} is the mass change at the cathodic potential limit: 0.1 V vs. Li, and Δm_0 is initial value in each cycle (= 0 μg cm^{-2}). The closer this value is to 1, the higher the reversibility. Again, the results are also strongly dependent upon anions in the electrolyte solutions. The $LiBH_4$/THF shows excellent reversibility over the entire cycle. It suggests that almost no SEI layer was formed and only adsorption state changes of ions were observed as the mass change during the cyclic voltammetry. On the other hand, $-\Delta m_{anodic}/\Delta m_{cathodic}$ in $LiPF_6$/EC–DEC shows negative values because the Δm increases even in the anodic scan. The surface layer continuously grows during the CV cycles. As for the LiTFSA-based electrolyte solutions, the reversibility gradually improves with cycling; suggesting that the stable SEI layer formed in the initial cycles prevents further decomposition of the electrolyte solution. Therefore, we suspect that the reversible peaks and mass change during the cyclic voltammetry (Figures 1c and 1d) are corresponding to adsorption/desorption of ions and solvent molecules. This trend supports the fact that LiTFSA is a functional additive for lithium-ion batteries.[50]

In order to characterize the surface layer, we also conducted XPS analyses of the electrodes prepared by these four electrolytes. The surface layer was formed on a copper electrode by a potentiostatic method. The electrode potential was maintained at 0.5 V vs. Li in the case of $LiBH_4$/THF. The potential is low enough to form the surface layer since it is lower than where the cathodic current was observed in the EQCM cyclic voltammetry. The electrode potential was maintained at 1.5 V vs. Li in the case of other electrolyte solutions to investigate the early stage of SEI formation process. Figures 3–6 show XPS spectra of these electrodes. Three stacked spectra in each graph represent the argon sputtering process. The spectra at the top of the chart correspond to the electrodes without argon sputtering. The spectra at the middle and bottom are corresponding to after the argon sputtering for 10 seconds and 30 seconds respectively. The detected signals are displayed by dotted lines, while the backgrounds, the deconvoluted peaks, and the sums are displayed by solid lines. The peak assignments for the spectra are carried out by referring multiple sources: the spectra we took with reference samples, NIST X-ray Photoelectron Spectroscopy Database, and past reports[16,51,52] and listed in Table I. Relative elemental composition is estimated by integration of peak area and listed in Table II.

The XPS spectra and the elemental composition for the $LiBH_4$/THF also prove that the $LiBH_4$/THF produces a tiny amount of the surface layer. Figure 3 shows the XPS spectra of the copper electrode treated in the $LiBH_4$/THF. The C 1s spectrum of the surface can be deconvoluted into four components, which derived from hydrocarbon contamination, polyether compounds, lithium alkyl carbonate ($ROCO_2Li$), and lithium carbonate (Li_2CO_3). The peak intensity of the C 1s spectra immediately decreases by the argon-ion etching. Also, Figure 3b shows that the O 1s peaks corresponding to ethers and carbonates mostly disappeared after the sputtering. It suggests that the layer in the $LiBH_4$/THF contains little organic compounds. On the other hand, we identified two inorganic species in the B 1s spectra shown in Figure 3d; the peaks at 188.0 eV and 191.5 eV are assigned to $LiBH_4$ and lithium metaborate ($LiBO_2$) respectively. The broad peak corresponding to residual $LiBH_4$ salts is observed only in the spectrum at the surface of the electrode. Even though the peak corresponding

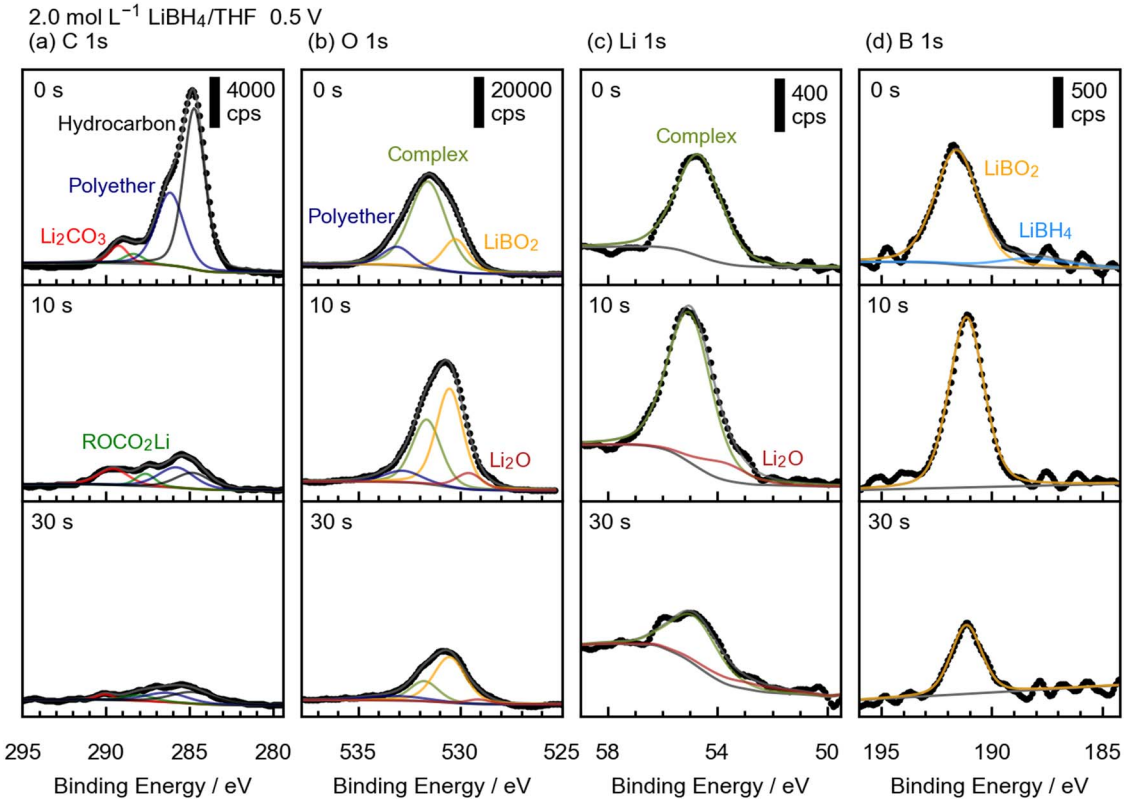

Figure 3. (a) C 1s, (b) O 1s, (c) Li 1s, and (d) B 1s XPS spectra of the copper electrode maintained at 0.5 V vs. Li for 24 hours in 2.0 mol L^{-1} $LiBH_4$ in THF.

to $LiBO_2$ remained even after the argon etching, the amount of the $LiBO_2$ is much smaller than carbon-based species, as shown in Table II. Furthermore, the atomic concentration of Cu for the $LiBH_4$/THF is much higher than that for the other three electrolyte solutions. Therefore, we think the XPS results are in good agreement with the EQCM results.

We also conducted the characterization of the surface layer derived from in the electrolyte solutions containing the conventional electrolyte salts. Even though the three samples are prepared at 1.5 V vs. Li, which is high electrode potential, the surface layers are formed on the copper electrodes. Figure 4 shows C 1s XPS spectra of the copper electrodes prepared in (a) $LiPF_6$/EC–DEC, (b) LiTFSA/EC–DEC, and (c) LiTFSA/diglyme. The C 1s XPS spectra for the $LiPF_6$/EC–DEC show the formation of the polyether-based surface layer; however, the signals immediately got weaker after the argon sputtering. As for the LiTFSA-based solutions, in contrast, the C 1s XPS spectra show that the surface layer containing $ROCO_2Li$ or Li_2CO_3 are formed. Since the peaks corresponding to $ROCO_2Li$ and Li_2CO_3 remain even after 30 seconds of the argon-ion sputtering, a significant amount of $TFSA^-$ anions and solvent molecules are reduced during the electrochemical process.

Figure 5 shows F 1s spectra for the three solutions. All the spectra have a peak at 685–686 eV assigned to LiF. The peak intensity of the LiF in the $LiPF_6$/EC–DEC is significantly higher than the other two electrolytes, and another peak corresponding to the residual salt is almost negligible. We also confirmed peaks at 56.0 eV, which can be assigned to LiF in Li 1s spectra, as shown in Figure 6. Also, Li and F are the main components of the surface layer in $LiPF_6$/EC–DEC, as shown in Table II. The facts indicate that the surface layer mostly consists of LiF.

Table II. Relative elemental composition based on the integrated peak intensity of the XPS spectra.

		Atomic concentration/%					
Electrolyte solution	Etching time/s	C 1s	O 1s	Li 1s	B 1s	F 1s	Cu 2p
2.0 mol L^{-1}	0	33.3	35.3	22.7	5.9		2.8
$LiBH_4$ in THF	10	9.7	35.0	33.3	5.6		16.4
	30	6.5	17.1	16.2	3.2		57.0
1.0 mol L^{-1}	0	4.1	3.1	47.4		45.3	0.1
$LiPF_6$ in EC–DEC	10	1.5	1.1	48.8		48.5	0.1
	30	1.6	1.3	47.4		49.5	0.2
1.0 mol L^{-1}	0	30.3	41.1	20.5		4.2	3.9
LiTFSA in EC–DEC	10	30.9	40.5	15.6		4.0	9.0
	30	24.1	38.1	25.5		3.9	8.4
1.0 mol L^{-1}	0	28.9	36.4	24.9		1.1	8.7
LiTFSA in diglyme	10	26.4	36.5	20.9		2.7	13.5
	30	23.8	32.0	25.8		1.7	16.7

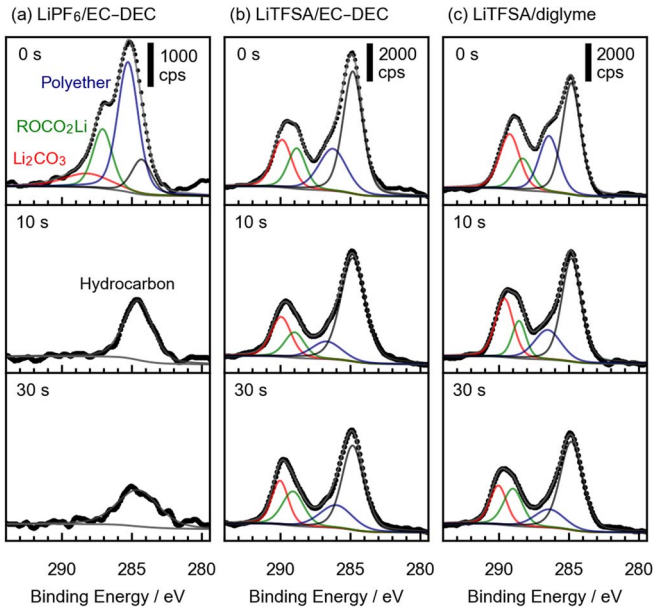

Figure 4. C 1s XPS spectra of the copper electrodes maintained at 1.5 V vs. Li in (a) 1.0 mol L^{-1} $LiPF_6$ in EC–DEC, (b) 1.0 mol L^{-1} LiTFSA in EC–DEC, and (c) 1.0 mol L^{-1} LiTFSA in diglyme.

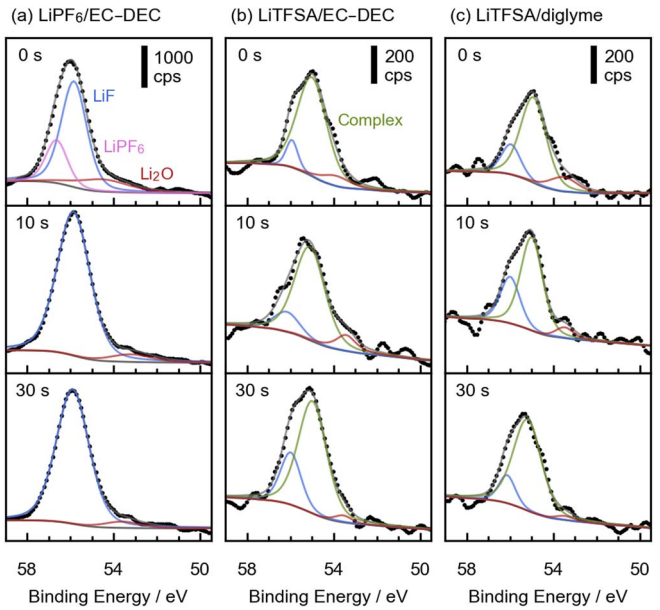

Figure 6. Li 1s XPS spectra of the copper electrodes at 1.5 V vs. Li in (a) 1.0 mol L^{-1} $LiPF_6$ in EC–DEC, (b) 1.0 mol L^{-1} LiTFSA in EC–DEC, and (c) 1.0 mol L^{-1} LiTFSA in diglyme.

In LiTFSA/EC–DEC, we observe peaks that derived from $TFSA^-$ anion in all the F 1s and Li 1s spectra, as shown in Figures 5b, 5c, 6b and 6c. The salts and decomposition products of the electrolyte seem to turn into layer components concertedly. Since the $TFSA^-$ anion derivatives are continuously detected after the argon sputtering in the case of the LiTFSA/EC–DEC, we assume a relatively porous organic layer is formed, compared with the LiTFSA/diglyme.

The LiF formation as the main component in the $LiPF_6$/EC–DEC is obviously due to the reduction of PF_6^- anions. Hydrofluoric acid (HF), typically contained as an impurity species in the $LiPF_6$/EC–DEC, may also contribute to the formation of the LiF layer. The EQCM measurement suggests that the reduction of the PF_6^- anions take place at the initial cathodic sweep of the cyclic voltammetry. Furthermore, the following cyclic voltammograms prove that the electrode surface is well passivated during the initial cycle. The results indicate that $LiPF_6$ preferably forms a dense LiF layer which suppresses further reductions of the anions and solvent molecules. In contrast, the surface layer formed in the LiTFSA-based solutions contains a significant amount of organic compounds, which is formed by decomposed $TFSA^-$ anions and solvent molecules. Therefore, the surface layer behaves like a polymer electrolyte, and the reversible current peaks are observed in the CV.

According to the XPS spectra, the surface layer characteristics are highly dependent upon the anions in the electrolyte solutions. The trend can be seen in the depth profiles of Cu 2p, as shown in Figure 7. For the $LiBH_4$/THF, the copper substrate immediately appears at the early stage of the argon etching. It shows that the surface layer is extremely thin even at 0.5 V vs. Li. The result is in good agreement with the EQCM findings. In the case of the $LiPF_6$/EC–DEC, the atomic concentration of Cu 2p is lower than 2% until the etching time reached to 60 s. However, it increases up to 75% after 5 minutes of the argon sputtering. Since the Cu 2p content after the sputtering process is close to that for the $LiBH_4$/THF, we think thin and dense LiF layer is formed in $LiPF_6$/EC–DEC. On the other hand, for the LiTFSA-based

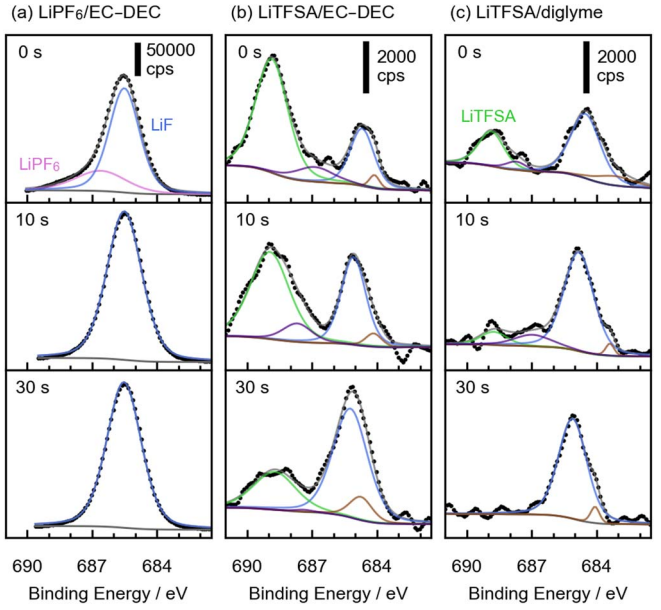

Figure 5. F 1s XPS spectra of the copper electrodes maintained at 1.5 V vs. Li in (a) 1.0 mol L^{-1} $LiPF_6$ in EC–DEC, (b) 1.0 mol L^{-1} LiTFSA in EC–DEC, and (c) 1.0 mol L^{-1} LiTFSA in diglyme.

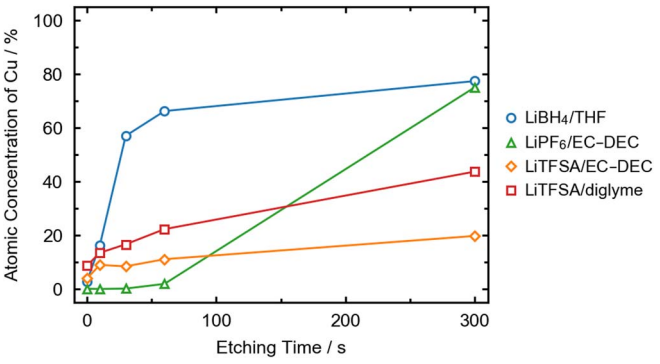

Figure 7. Cu 2p XPS depth profiles of the copper electrodes after the surface layer formation process. The atomic concentrations are estimated based on the integrated peak intensity.

electrolyte solutions, the atomic concentrations of Cu 2p gradually increases as etched, but the Cu content is still <50% after the argon etching.

There remains a question concerning the amount of the surface layer because the EQCM and XPS results have some contradiction. The EQCM results suggest that the $TFSA^-$ anion forms a relatively small amount of the surface layer compared with the PF_6^- anion. On the other hand, the depth profiles of the XPS spectra indicate that the surface layer formed in the $LiPF_6$/EC–DEC is thinner than that formed in the LiTFSA–based solutions. We think it is due to the kinetics of the surface layer formation process. The XPS samples were exposed in the electrolyte solution for 24 hours while the measurement time of the EQCM is <1000 seconds. Further studies concerning the reaction kinetics of the surface layer formation process should be done in the future.

Conclusions

In the present study, we investigate the amount and the chemical composition of the surface layer formed in four electrolyte solutions using EQCM and XPS. The EQCM and XPS result quantitatively reveal that negligible amount of surface layer is formed at 0.5 V vs. Li in 2.0 mol L^{-1} $LiBH_4$ in THF solution. The EQCM cyclic voltammograms represent that the amount of the layer in the $LiBH_4$ solution is a hundred times smaller than the other three electrolytes. Hence we think the $LiBH_4$ solution forms a pseudo-SEI-free interphase, which significantly improves the cycling performance of the intermetallic anodes, as we previously reported.

On the other hand, the other three conventional electrolytes form the SEI layer even at the high electrode potential: 1.5 V vs. Li. In 1.0 mol L^{-1} $LiPF_6$ in EC–DEC (50:50 vol%) solution, the PF_6^- anions are rapidly reduced to form a thin, dense, and stable LiF layer. The surface layers in the LiTFSA-based electrolyte solutions mainly contain organic components such as lithium alkyl carbonate and polyether. The organic surface layer gradually grows during the long-time potentiostatic measurement.

According to the above results, we conclude that the primary component of the SEI layer is highly dependent on the choice of anion species. We also prove that the $LiBH_4$-based electrolyte forms pseudo-SEI-free interphase. We believe the variety of the SEI design may enable us to maximize the electrochemical properties of high-energy anodes such as lithium metal and intermetallic anodes.

Acknowledgment

The present study was financially supported by Japan Science and Technology Agency PRESTO grant Number JPMJPR13CA, JSPS KAKENHI grant Number JP16H06055, JP19H02816, and Tokyo Ohka Foundation for the Promotion of Science and Technology.

ORCID

Hidetoshi Sonoki https://orcid.org/0000-0002-3728-361X
Masaki Matsui https://orcid.org/0000-0003-1499-7457
Nobuyuki Imanishi https://orcid.org/0000-0003-1424-0729

References

1. B. Scrosati and J. Garche, *J. Power Sources*, **195**, 2419 (2010).
2. T. Horiba, *Proc. IEEE*, **102**, 939 (2014).
3. E. A. Olivetti, G. Ceder, G. G. Gaustad, and X. Fu, *Joule*, **1**, 229 (2017).
4. W. Xu, J. Wang, F. Ding, X. Chen, E. Nasybulin, Y. Zhang, and J.-G. Zhang, *Energy Environ. Sci.*, **7**, 513 (2014).
5. M. N. Obrovac and V. L. Chevrier, *Chem. Rev.*, **114**, 11444 (2014).
6. E. Peled, *J. Electrochem. Soc.*, **126**, 2047 (1979).
7. J. G. Thevenin and R. H. Muller, *J. Electrochem. Soc.*, **134**, 273 (1987).
8. K. Kanamura, H. Tamura, S. Shiraishi, and Z. Takehara, *J. Electrochem. Soc.*, **142**, 340 (1995).
9. E. Peled, D. Golodnitsky, and G. Ardel, *J. Electrochem. Soc.*, **144**, L208 (1997).
10. D. Aurbach and Y. Cohen, *J. Electrochem. Soc.*, **143**, 3525 (1996).
11. K. Naoi, M. Mori, Y. Naruoka, W. M. Lamanna, and R. Atanasoski, *J. Electrochem. Soc.*, **146**, 462 (1999).
12. A. Varzi, R. Raccichini, S. Passerini, and B. Scrosati, *J. Mater. Chem. A*, **4**, 17251 (2016).
13. D. Aurbach, Y. Gofer, and J. Langzam, *J. Electrochem. Soc.*, **136**, 3198 (1989).
14. K. Kanamura, S. Shiraishi, and Z. Takehara, *J. Electrochem. Soc.*, **143**, 2187 (1996).
15. H. Ota, K. Shima, M. Ue, and J. Yamaki, *Electrochim. Acta*, **49**, 565 (2004).
16. H. Kuwata, H. Sonoki, M. Matsui, Y. Matsuda, and N. Imanishi, *Electrochemistry*, **84**, 854 (2016).
17. H. Wang, M. Matsui, H. Kuwata, H. Sonoki, Y. Matsuda, X. Shang, Y. Takeda, O. Yamamoto, and N. Imanishi, *Nat. Commun.*, **8**, 15106 (2017).
18. M. Arakawa, S. Tobishima, Y. Nemoto, M. Ichimura, and J. Yamaki, *J. Power Sources*, **43–44**, 27 (1993).
19. M. Rosso, C. Brissot, A. Teyssot, M. Dollé, L. Sannier, J.-M. Tarascon, R. Bouchet, and S. Lascaud, *Electrochim. Acta*, **51**, 5334 (2006).
20. J. Becking, A. Gröbmeyer, M. Kolek, U. Rodehorst, S. Schulze, M. Winter, P. Bieker, and M. C. Stan, *Adv. Mater. Interfaces*, **4**, 1700166 (2017).
21. U. Kasavajjula, C. Wang, and A. J. Appleby, *J. Power Sources*, **163**, 1003 (2007).
22. H. Li, X. Huang, L. Chen, Z. Wu, and Y. Liang, *Electrochem. Solid-State Lett.*, **2**, 547 (1999).
23. L. Hu, H. Wu, S. S. Hong, L. Cui, J. R. McDonough, S. Bohy, and Y. Cui, *Chem. Commun.*, **47**, 367 (2011).
24. A. Magasinski, B. Zdyrko, I. Kovalenko, B. Hertzberg, R. Burtovyy, C. F. Huebner, T. F. Fuller, I. Luzinov, and G. Yushin, *ACS Appl. Mater. Interfaces*, **2**, 3004 (2010).
25. S. Komaba, K. Shimomura, N. Yabuuchi, T. Ozeki, H. Yui, and K. Konno, *J. Phys. Chem. C*, **115**, 13487 (2011).
26. L. Chen, K. Wang, X. Xie, and J. Xie, *J. Power Sources*, **174**, 538 (2007).
27. N.-S. Choi, K. H. Yew, K. Y. Lee, M. Sung, H. Kim, and S.-S. Kim, *J. Power Sources*, **161**, 1254 (2006).
28. S. Dalavi, P. Guduru, and B. L. Lucht, *J. Electrochem. Soc.*, **159**, A642 (2012).
29. J.-S. Bridel, S. Grugeon, S. Laruelle, J. Hassoun, P. Reale, B. Scrosati, and J.-M. Tarascon, *J. Power Sources*, **195**, 2036 (2010).
30. C. C. Nguyen and B. L. Lucht, *J. Electrochem. Soc.*, **161**, A1933 (2014).
31. H. Kuwata, M. Matsui, H. Sonoki, Y. Manabe, N. Imanishi, and M. Mizuhata, *J. Electrochem. Soc.*, **165**, A1486 (2018).
32. D. Aurbach and A. Zaban, *J. Electroanal. Chem.*, **393**, 43 (1995).
33. T. Kawaguchi, K. Shimada, T. Ichitsubo, S. Yagi, and E. Matsubara, *J. Power Sources*, **271**, 431 (2014).
34. K. Kanamura, H. Takezawa, S. Shiraishi, and Z. Takehara, *J. Electrochem. Soc.*, **144**, 1900 (1997).
35. R. Dedryvère, S. Laruelle, S. Grugeon, L. Gireaud, J.-M. Tarascon, and D. Gonbeau, *J. Electrochem. Soc.*, **152**, A689 (2005).
36. A. Zaban, E. Zinigrad, and D. Aurbach, *J. Phys. Chem.*, **100**, 3089 (1996).
37. G. Sauerbrey, *Z. Phys.*, **155**, 206 (1959).
38. J. D. Hunter, *Comput. Sci. Eng.*, **9**, 90 (2007).
39. W. McKinney, in *Proceedings of the 9th Python in Science Conference (SciPy 2010)*, S. van der Walt and J. Millman, Editors, vol. **445**, p. 51, Austin, TX (2010).
40. A. Debart, L. DuPont, P. Poizot, J.-B. Leriche, and J.-M. Tarascon, *J. Electrochem. Soc.*, **148**, A1266 (2001).
41. E. Peled, D. Golodnitsky, C. Menachem, and D. Bar-Tow, *J. Electrochem. Soc.*, **145**, 3482 (1998).
42. J. B. Goodenough and Y. Kim, *J. Power Sources*, **196**, 6688 (2011).
43. H. Lee, J.-J. Cho, J. Kim, and H.-J. Kim, *J. Electrochem. Soc.*, **152**, A1193 (2005).
44. I. T. Lucas, E. Pollak, and R. Kostecki, *Electrochem. Commun.*, **11**, 2157 (2009).
45. L. Martin, H. Martinez, D. Poinot, B. Pecquenard, and F. Le Cras, *J. Power Sources*, **248**, 861 (2014).
46. M. Ayache, S. F. Lux, and R. Kostecki, *J. Phys. Chem. Lett.*, **6**, 1126 (2015).
47. E. Peled and S. Menkin, *J. Electrochem. Soc.*, **164**, A1703 (2017).
48. D. Aurbach, *J. Power Sources*, **89**, 206 (2000).
49. K. Xu, *Chem. Rev.*, **104**, 4303 (2004).
50. V. Sharova, A. Moretti, T. Diemant, A. Varzi, R. J. Behm, and S. Passerini, *J. Power Sources*, **375**, 43 (2018).
51. T. Eriksson, A. M. Andersson, A. G. Bishop, C. Gejke, T. Gustafsson, and J. O. Thomas, *J. Electrochem. Soc.*, **149**, A69 (2002).
52. H. Ota, Y. Sakata, X. Wang, J. Sasahara, and E. Yasukawa, *J. Electrochem. Soc.*, **151**, A437 (2004).